REPORT DOCUMENTATION PAGE

Form Approved
OMB No. 0704-0188

1. REPORT DATE *(DD-MM-YYYY)*	2. REPORT TYPE	3. DATES COVERED *(From - To)*
20-06-2005	Journal Article	

4. TITLE AND SUBTITLE

Measurements in an Acoustically-Driven Coaxial Jet under Sub-, Near-, and Supercritical Conditions (PREPRINT)

5a. CONTRACT NUMBER

5b. GRANT NUMBER

5c. PROGRAM ELEMENT NUMBER

6. AUTHOR(S)
Dustin W. Davis and Bruce Chehroudi (Engineering Research Consultants, Inc.)

5d. PROJECT NUMBER
2308

5e. TASK NUMBER
0533

5f. WORK UNIT NUMBER

7. PERFORMING ORGANIZATION NAME(S) AND ADDRESS(ES)

Air Force Research Laboratory (AFMC)
AFRL/PRSA
10 E. Saturn Blvd.
Edwards AFB CA 93524-7680

8. PERFORMING ORGANIZATION REPORT NUMBER

AFRL-PR-ED-JA-2005-271

9. SPONSORING / MONITORING AGENCY NAME(S) AND ADDRESS(ES)

Air Force Research Laboratory (AFMC)
AFRL/PRS
5 Pollux Drive
Edwards AFB CA 93524-7048

10. SPONSOR/MONITOR'S ACRONYM(S)

11. SPONSOR/MONITOR'S NUMBER(S)
AFRL-PR-ED-JA-2005-271

12. DISTRIBUTION / AVAILABILITY STATEMENT

Approved for public release; distribution unlimited

13. SUPPLEMENTARY NOTES
Submitted to Journal of Propulsion and Power

14. ABSTRACT

An experimental investigation was conducted on a coaxial jet, similar to those used in cryogenic liquid rockets, under sub-, near-, and supercritical pressures, with the ultimate intent of gaining a better understanding of an aspect of combustion instability that pertains to interactions of an externally-imposed acoustic field with the jet. Past research works on this subject have shown both the relevance and importance of geometrical changes in an injector's exit-area and its nearby physical and fluid mechanical processes. On this basis, special attention is paid in collecting spatially-resolved time averaged temperatures and documenting the aforementioned interactions at the exit of this injector. Short-duration and high-speed framing digital images provided information on the behavior of this jet under a variety of conditions. Mean and rms values of the "dark-core" length fluctuations were measured from the acquired images via a computer-automated method and the ensuing results are discussed. There appears to be a good correlation between this length and the outer-to-inner jet momentum ratio, but the form of this dependence was found to be different at subcritical pressures than the rest of the conditions. The rms values of the dark-core length fluctuations suggested a possible explanation for the observed improvement in instability limit at increasingly higher outer-to-inner jet velocity ratios.

15. SUBJECT TERMS

16. SECURITY CLASSIFICATION OF:			17. LIMITATION OF ABSTRACT	18. NUMBER OF PAGES	19a. NAME OF RESPONSIBLE PERSON
					Dr. Douglas G. Talley
a. REPORT	b. ABSTRACT	c. THIS PAGE			19b. TELEPHONE NUMBER *(include area code)*
Unclassified	**Unclassified**	**Unclassified**	A	35	(661) 275-6174

Measurements in an Acoustically-Driven Coaxial Jet under Sub-, Near-, and Supercritical Conditions

Dustin W. Davis* and Bruce Chehroudi†
Engineering Research Consultants, Inc. , Edwards AFB, CA, 93524

An experimental investigation was conducted on a coaxial jet, similar to those used in cryogenic liquid rockets, under sub-, near-, and supercritical pressures, with the ultimate intent of gaining a better understanding of an aspect of combustion instability that pertains to interactions of an externally-imposed acoustic field with the jet. Past research works on this subject have shown both the relevance and importance of geometrical changes in an injector's exit-area and its nearby physical and fluid mechanical processes. On this basis, special attention is paid in collecting spatially-resolved time averaged temperatures and documenting the aforementioned interactions at the exit of this injector. Short-duration and high-speed framing digital images provided information on the behavior of this jet under a variety of conditions. Mean and rms values of the "dark-core" length fluctuations were measured from the acquired images via a computer-automated method and the ensuing results are discussed. There appears to be a good correlation between this length and the outer-to-inner jet momentum ratio, but the form of this dependence was found to be different at subcritical pressures than the rest of the conditions. The rms values of the dark-core length fluctuations suggested a possible explanation for the observed improvement in instability limit at increasingly higher outer-to-inner jet velocity ratios.

Nomenclature

C = constant

D = diameter with subscripts

L = length of dark core, length of injector tube

M = momentum flux ratio of outer jet to inner jet

* Ph.D. Candidate Penn State University, and Scientist, AFRL/PRSA/ERC, 10 E. Saturn Blvd., AIAA Member.
†Corresponding Author, Sr. Scientist, AFRL/PRSA/ERC,10 E. Saturn Blvd. ChehroudiB@aol.com, AIAA Member.

m = mass flow rate

n = exponent of M

P = pressure

R = radius with subscripts

R_h = hydraulic radius of outer jet, equal to the gap width

T = temperature

U = velocity

VR = velocity ratio of outer jet to inner jet

μ = viscosity

ρ = density

σ = surface tension

Subscripts

1,2,3,4 = four diameters or radii of the coaxial injector from the smallest to largest values

i = subscript denoting inner jet

o = subscript denoting outer jet

I. Introduction

COMBUSTION instability is a problem that has been observed with liquid rocket engines since the late 1930's, see Culick and Yang[1]. Three types of combustion instabilities have been identified based on the frequencies involved. Low frequency instability (chugging) is when the wavelength is much longer than the characteristic dimension of the chamber and the feed system. Generally, chugging frequencies are less than a few hundred Hz. High frequency instability (screaming) is the second type which is also referred to as acoustic instability due to the closeness of the measured pressure oscillation frequencies to the computed acoustic resonance modes of the thrust chamber. An intermediate frequency (buzz) consists of the lumping of the instabilities that do not fall into either chugging or screaming categories, see Harrje and Reardon[2].

Typically, for cryogenic propellant systems consisting of liquid oxygen (LOX) – hydrogen (H_2), a shear-coaxial type injector is used. Examples are the designs presently employed in the Space Shuttle Main Engine (SSME) or the Ariane 5 Vulcain engine (Vingert et al.[3]), and the RL-10 and J-2 engines from the late 1950's (Hulka and Hutt)[4]. One method of eliminating the acoustic instability in liquid rocket engines is to modify the spray combustion field,

which is usually achieved through modifications to the injector design, see Harrje and Reardon[2]. One such modification to the Ariane 5 Vulcain reported by Vingert et al.[3], increased the mean droplet diameter size and improved the stability of the engine. These changes to the injector design ultimately affect the mixing characteristics of the propellant streams in the thrust chamber. The fundamental physics of the breakup of a liquid jet and its subsequent mixing with other fluids have been studied since Rayleigh's study in 1878[5]. Much progress has been made since then, and as a result we are approaching a fundamental understanding of fluid jet break up and atomization processes, see for example Lefebvre[6]. However, full understanding is not yet available (Eroglu et al.[7]). A review of liquid jet atomization processes from a coaxial-type injector has recently been presented by Lasheras and Hopfinger[8], discussing some of the more recent developments in this area.

The importance of interactions between the acoustic field and a fluid jet in the context of combustion instability has been realized for some time. This notion arises from designers' ability to bring about improvements in engine stability through modifications in injector designs. Combustion in a rocket engine is controlled by, or at least intimately related to, the jet breakup and mixing processes of the oxidizer and fuel streams. Some early works on the interaction of high-amplitude acoustic waves with fluid jets were done by Miesse.[9] Miesse excited atmospheric-pressure round water jets with a high-intensity acoustic field and observed a decrease in the breakup length of the jet. Buffum and Williams[10] also investigated the effects of a transverse acoustic wave at frequencies in the range of 100 to 500 Hz and at amplitudes up to 161 dB on round liquid jets, measuring jet lateral deflection from its stable position. They observed an induced deflection of the jet at acoustic amplitudes above 130 dB.

Hulka and Hutt[4] have compiled an extensive review of coaxial injectors used in reported LOX/H_2 rocket engine stability tests by others with the objective of identifying key injector design or operating conditions contributing to combustion instability in these engines. What they found, and also reported by others, was that the outer-to-inner jet exit velocity ratio played a key role in many of the studies defining stability. Although much scatter is seen in the accumulated results, generally speaking, high velocity ratio values tended to improve engine stability limits. For a wide variety of injector designs and operating conditions, a velocity ratio of about 10 was the maximum where combustion instability occurred, with the exception of the M-1 engine. Additionally, they point out that a velocity ratio as low as 1 has been stable and a ratio as high as 15 was required to stabilize the M-1 engine.

One method for LOX/H_2 rocket engine stability rating is to perform so-called "temperature-ramping" of the H_2 (flowing into the outer annular region of the coaxial injector) by reducing its temperature from a high value to low

enough temperature until an onset of instability in the engine is measured. An engine, injector or combined injector/engine design as a system, which produces a lower H_2 temperature at the onset of the instability, implies a more stable system. One issue with the data accumulated by Hulka and Hutt[4] is that the original researchers reporting the results usually measured propellant temperatures well upstream of the injector exit area which could provide calculated velocity ratios quite different from its true values at the exit. Additionally, under near- or supercritical conditions, as also pointed out by them[4], small changes in temperature, even if measured at the injector exit plane, can produce large changes in density, strongly affecting the accuracy of estimates for velocity ratios. It is this lack of accurate information that partly motivated the current authors to initiate research providing details and accurate measurements of temperature radial profiles at the exit of a coaxial injector design, something we are unaware has ever been undertaken before to the detail presented here.

As indicated by Wanhainen et al.,[11] although velocity ratio seems to serve quite well as a correlating parameter, it is difficult to relate it to a physical combustion model and it may indeed be symbolic of other fundamental parameters. It is our ultimate intention to shed some light and contribute towards such a key physical understanding. It is also interesting to mention a related work reported by Hiedmann[12] in a circular combustor with LOX jets injecting radially from the side walls of the combustor. The H_2 streams were introduced into the chamber in a diffuse manner, somewhat similar to a coaxial design. The combustion instability was induced by injection of nitrogen streams circumferentially to be perpendicular to the LOX injection direction. In images, Hiedmann[12] observed that the length of the LOX dark core decreased during every screaming combustion instability event. This motivated us to pay special attention to the observed “dark-core” impression of the jets as seen in our studies.

Therefore, to gain physical insight on the effects of an externally-imposed acoustic field on the flow and thermodynamic conditions of a coaxial jet near its exit area, experiments were designed and conducted to have as many of the key features of a LOX/H_2 rocket engine as possible in a cold flow environment. Chehroudi and co-workers[13,14] have assembled a single-element coaxial-jet non-combusting test rig operating at cryogenic temperatures, transcritical temperature ranges, sub- to supercritical pressures, realistic outer-to-inner jet velocity ratios, and activation of an acoustical field inside the test chamber simulating one important aspect of the environment when combustion instability intensifies. Additional details on the development of this work can be found in previous papers by Davis and Chehroudi[13-15] in which a coaxial jet injector was designed, based on a well-characterized single-jet injector investigated by Chehroudi and coworkers.[16-20]

II. Experimental Facility

The experimental facility, previously described by Chehroudi and co-workers[13-20], has undergone considerable upgrades and modifications in order to improve the quality of the data and expand the operating range of the facility. A schematic diagram of the key components of the improved facility is shown in Fig. 1, along with a photograph of the inner chamber and injector tip is seen in Fig. 2. Gaseous nitrogen (GN2) from the laboratory feed line was used to pressurize the test chamber and also to produce the jets issuing from a coaxial injector's center post (or inner tube) and its outer annular coaxial region. The feed GN2 flow rates, used to produce the inner and outer jets, are measured separately with Porter Mass flow meters. Subsequently, the GN2 streams flow through a series of heat exchangers (HX) to be cooled, see Fig. 1. These HXs are cooled by the "facility liquid nitrogen (LN2)" stored in a cryogenic tank outside the test cell. The GN2 feeding the inner jet is passed through a counter-flow HX cooled to below the critical temperature. The exiting nitrogen (now LN2) from the center-post HX is then directly sent to the injector. The GN2 for the outer flow passes through two HXs (primary and secondary) before it is directed to the injector. The facility LN2 flow rate to the secondary HX is adjusted to produce a desired temperature of the outer jet at the exit plane of the injector. Independent control over the outer jet exit temperature was not previously available in our facility. For reference, the critical temperature and pressure of nitrogen are 126.2 K and 3.4 MPa, respectively.

The injector used in this study (Fig. 2(b)), the details of which were previously given by Davis and Chehroudi,[13-15] produces a cryogenic jet that is injected through a sharp-edged stainless steel inner tube having a length (L) of 50 mm, an inner diameter (D_1) of 0.508 mm, an outer diameter of the inner tube (D_2) of 1.59 mm, an inner diameter of the outer tube (D_3) of 2.42 mm, and an outer diameter of the outer tube (D_4) of 3.18 mm. The resulting L/D_1 is 100, considered sufficient to ensure a fully-developed turbulent pipe flow at the injector exit plane. The gap width (R_h) between the inner and outer tubes, defining the annular region, was 0.415 mm. The injector had a bias measured to 8% of the mean gap width and the inner tube was recessed by about ~ 0.5 D_1.

The chamber is designed to withstand pressures up to 14 MPa. There is a smaller rectangular-shaped chamber inside the main chamber (see Fig 2 (a)). The purpose of the main chamber is to contain the pressure whereas that of the inner one is to act as a cavity resonator at the same pressure as the main chamber, with the intention of achieving the highest amplitude of the acoustically-induced velocity in the vicinity of the jet. The inner-chamber cavity was driven by a piezo-siren, specially-designed by Hersh Acoustical Engineering, Inc. This device is capable

of producing sound pressure levels (SPL) of up to 180 dB (measured in an impedance tube) at resonant frequencies lying between 1000 to 8000 Hz and at pressures up to 14 MPa. The siren is physically coupled to the inner chamber via a circular-to-rectangular transition piece to guide the acoustic waves into the measurement zone of the inner chamber. Actual SPL levels in the inner chamber were between 161 dB and 171 dB at its first two resonance frequencies of 3.0 kHz and 5.2 kHz. The resonance frequencies change slightly with changes in chamber pressure and temperature.

Radial temperature profiles of the jet at the exit of the injector were measured with a Type-E thermocouple (TC) installed on a traversing stage that protrudes into the inner chamber region (see Fig. 3). The best estimate of the measurement accuracy of a standard calibration of the Type-E TC within our range of interest is on the order of ± 5 K. This is considered too large, especially near the critical point of nitrogen, producing large uncertainties in density and injection velocity calculations. The uncertainty is due to composition variations of the particular bead and wire materials used within the manufacturing specification. Typically, a curve fit to the calibration data over a large range is quite adequate and has only a few degrees of uncertainty at room temperatures or warmer. However, at cryogenic temperatures, the uncertainties grow because the output voltage from a TC decreases at low temperatures and becomes a larger portion of the output signal. Therefore, it was necessary to re-calibrate the TCs in-house to mitigate these effects. The calibration was performed against a precision platinum resistance temperature detector (Pt-RTD) over a range of 77 to 300 K. The Pt-RTD was manufactured and calibrated by Hart and had an accuracy of ±0.04K. No Pt-RTD was available in the small size required to make measurements in the jet, but the size was unimportant for the calibration procedure itself. The maximum estimated uncertainty over the range of interest for the re-calibrated thermocouples was ± 0.8 K. To assess the effect of the TC on the on the temperature field in the vicinity of the TC, CFD calculations were performed, and determined to be insignificant.

The addition of the exit-plane temperature measurement system was a significant improvement to the facility. Previous temperature measurements by Davis et al.[14] were performed with the standard calibration of a Type E TC which had a large bead diameter of approximately 0.4mm, and had no mechanism for removing the bead from the jet flow without opening the main chamber. This means that no images could be acquired during temperature measurements and another repeat run was required to accumulate such information. Additionally, the improved temperature measurement system uses a TC with a much smaller bead diameter than before (~0.1mm), which introduces less disturbance to the jet flow, particularly for the inner-jet temperature measurements. Also, the TC is

attached to a traversing mechanism, which permits measurements of radial profiles at a fixed axial distance of 0.28 D_1 downstream of the injector exit plane. Once temperature measurements are made, the TC can be traversed out of the flow far from the coaxial jet area, enabling imaging of the undisturbed jet in the same run.

Backlit images (12 bit) of the coaxial jet were taken at 10 Hz frame rate with resolution of 1280x1024 pixels using a PixelFly CCD camera manufactured by the Cooke Corporation. A General Radio Strobotac® strobe light was used for illumination purposes. The image was defined by the strobe flash duration of approximately 0.5 μs. Additionally, for some of the conditions, images were taken with a Phantom CMOS camera model version 5.1, manufactured by the Vision Research Company. The Phantom camera has the capability of producing 10-bit images at 93 kHz. However, in this study, and to increase the clarity of the features, the framing rate was set to 18 kHz at a resolution of 256x128 pixels. For this case, the images were backlit with a continuous light source, and were defined by the exposure time of the camera at 2μs duration. Unfortunately, the Phantom camera was acquired for a short time during the latter part of the project and was not used for all the conditions presented here.

The operation of a typical test consisted of a cool-down process for a certain period, allowing establishment of a steady-state condition for the entire facility including the plumbing system and the chamber. Once this condition was reached, radial traverses towards the coaxial jet centerline were made for temperature measurements, starting from a distance sufficiently far away from the jet to establish a background chamber temperature value. Measurements continued past the centerline until a large enough increase in temperature was observed, and sufficient data collected, to allow determination of a true jet centerline position. The TC traversing mechanism was then pulled entirely away from the jet area until it stopped near the wall of the inner chamber. With the TC clearing the path of the jet, images were taken while the acoustic driver was off, immediately followed by a set of images when the driver was operating and tuned to the first and second resonance frequencies of the inner chamber. Only 30 images were recorded when the PixelFly camera was in use. In contrast, the Phantom camera collected a large set of images of up to a 1000 for each condition.

III. Experimental Results and Discussion

The experimental matrix was organized to enable comparisons between results at different outer-to-inner jet velocity ratios. Thermodynamic conditions of the jet at the exit of the injector, calculated from temperature measurements, are shown in Fig. 4. The number near each of the data points in Fig. 4 represents the case number in

Table 1. Because of a large variation in density with small changes in temperature near the critical point (see Fig 4), two nominal outer-jet temperatures (around 135–140 K (low) and around 185–200 K (high)) were selected, and then the jet's mass flow rates were varied to obtain a desired outer-to-inner jet velocity ratio. References to these cases are made as "low" and "high" temperatures and should be clear in the context of the discussion.

A. Temperature Measurements

Radial profiles of the coaxial jet averaged temperature were measured at a normalized axial location (x/D_1) of about 0.28 from the injector exit plane (i.e., the exit edge of the outer tube) using a Type-E thermocouple as described above. Figure 5 shows the measured temperature and the associated density radial profiles computed using the NIST REFPROP[21] program accepting the radial temperature profile and chamber pressure as input data. The horizontal axis is radial distance measured from the jet centerline and is normalized by the inner-tube inside radius. The top, middle, and bottom rows in Fig. 5, are at the chamber pressures of 1.5 (subcritical), 3.5 (near-critical), 4.9 (supercritical) MPa, respectively. Scales for temperature profiles are read from the left axis and those for densities from the right axis. The left and right columns in Fig. 5 are at the low (~135 – 140 K) and high (~185 – 200 K) outer-jet temperatures respectively. The solid lines and symbols represent measured temperature profiles, and the dashed lines and hollow symbols show computed densities.

An attribute that the temperature profiles in Fig. 5 possess is that there are three distinct zones where the temperature gradient is fairly small: the core or region near the centerline of the jet, the region that defines the flow of the outer jet, and the far-field inner-chamber environment. The temperatures in these three regions were used to compute physical properties such as densities and viscosities, which in turn were used to compute quantities such as velocity, momentum, and their appropriate ratios.

At a given subcritical chamber pressure (i.e., 1.5 MPa, the top row in Fig. 5. Figs 5 a and b), both the temperature and density profiles representing the core region of the inner jet at the injector exit area are flat in shape, producing "top-hat" density profiles. The profiles then sharply change to quite different values, typical of a transition from a liquid to a gas phase, as expected. Note that for the low outer-jet temperature case, and at the measured axial location, this constant core temperature value penetrates well beyond the inner-tube radius, up to about r/R_1 of 2.5, independent of the velocity ratios used. Under this condition, variations of the velocity ratio have no impact on the radial extent of the inner jet as defined by either the temperature or density profiles. Also, small variations in the outer jet temperature have no effect on the calculated values for densities. However, at the higher

outer-jet temperature in Fig. 5b, the radial extent or penetration of the inner jet is strongly affected by the value of the outer-to-inner velocity ratio, primarily due to the increased heat transfer to the inner jet from the outer jet, both inside and immediately outside the injector. Note that the outer jet temperature is controlled manually by changes in the LN2 flow rate to the secondary HX, and the manual nature of this control system accounts for the variations seen in the outer jet temperatures. The variability of the inner-chamber temperature at the far field is related to changes in several factors, including mass flow rates of all nitrogen streams into the inner-chamber, their respective temperatures, and the length of time spent running the experiment (see Fig. 5b). Under the higher outer-jet temperature shown in Fig. 5b, the HX control system was able to maintain this temperature at a reasonably constant value and, again, small changes in temperature has no impact on the calculated densities.

As the chamber pressure is elevated to a near-critical value (i.e. 3.5 MPa, the middle row of Figs.5c and d), the "top-hat" nature of the radial profiles is lost and more rounded shapes are observed, perhaps due to drastic changes of the heat transfer characteristics inside the tube under elevated, especially near-critical, conditions. Additionally, the temperature of the core (of the jet) at the centerline is greater than the corresponding temperatures at the subcritical pressure discussed above. The density increase within the outer-jet zone from that of the far-field chamber value, especially at lower outer-jet temperature, is quite larger and more noticeable than that observed under subcritical pressures (see Figs. 5a &b). It is also noted that for the "case 19" plot (Fig. 5c), the temperature at the centerline is slightly higher (by approximately 5 K) than all other cases, causing the density profile to exhibit its maximum value at a slightly off-axis radial location. It is believed that the thermocouple may have moved off the plane defining a diameter to a plane defining a chord of the circular cross-section of the jet as the centerline was approached during a traverse operation. However, this remains to be verified in the future.

Further increase in chamber pressure to a supercritical condition (i.e., 4.9 MPa, the bottom row of Figs. 5e & f) leads to an insignificant change in the qualitative behavior of the profiles as compared to the 3.5 MPa case. Again, a strong contrast is seen between the far-field chamber and outer-jet densities, indicating sensitivity of the density to small changes in temperature under this condition. It is also noticed that at all velocity ratios, the value of the centerline temperature at the higher outer-jet temperature (Fig. 5f) is supercritical (i.e. > 126.2 K), whereas it is subcritical for all other cases in Fig. 5. For the lower outer-jet temperature cases, the difference in density between the outer-jet region and the far-field value is in excess of 200 kg/m^3, which makes this feature easily observable in images of the jet, but does not permit easy and clear distinction of the inner jet dark core areas.

B. Flow Visualization

Flow visualization of the jet with backlit photography provides many details about the flow structure and was used here to catalogue the coaxial jet behavior and its responses to the acoustic field. Figures 6, 7, and 8 are sample images of the coaxial jet under different conditions discussed in the ensuing paragraphs. The scale presented in Fig. 6(ii) is the same for Figs. 6(i) and 7. One prominent feature of these images is the so-called "dark core", which represents the high-density region of the inner jet. In these images, the inner jet has a much higher density than anywhere else in the field, thus minimizing the light penetration and causing it to appear dark and black. In many of the conditions, identification of the outer jet is made difficult because of the low density and low density gradient between the outer jet and the inner-chamber environment. However, under some conditions (see Fig. 5 at the low temperature for near- and super-critical conditions), the density and the density gradient are large enough to easily distinguish the periphery of the outer jet.

Figure 6(i) shows realizations of the coaxial jet under a subcritical chamber pressure and low outer-jet temperature. From left to right, in both rows, they correspond to cases 1 to 4 in Table 1. For the top row, Figs. 6(i) a to d, the acoustic driver is *off* and the bottom row, Figs. 6(i) e to h, shows the corresponding images when the acoustic driver is turned *on*. Images in the same column correspond to the same operating conditions and were taken at the same test run. The velocity ratio increases from left to right in Fig.6(i), while the inner-jet velocity is approximately constant. At the lowest velocity ratio (Fig. 6(i)a), the breakup of the jets appears to fall into the non-axisymmetric Rayleigh category, and the next higher velocity ratio (Fig. 6(i)b) is of the membrane-breakup type, even though the aerodynamic Weber number is much greater than what was observed for water-into-air injection by Faragó and Chigier[22]. At the next two higher velocity ratios (Figs. 6(i)c and d) a fiber-type breakup is observed with a pulsating mode. The exit width of the dark core is noticeably thinner for the case 2 (Fig. 6(i)b). If one compares the width of the high-density region defined in Fig. 5b with those of the dark core at the exit plane of the injector, the same trend will be observed. Upon an increase in velocity ratio, the atomization process is enhanced, which is qualitatively visible from the decrease in droplet sizes, particularly in high magnification images.

Comparing the top and bottom row images, a clear effect of the acoustic field is noticed for all four conditions in Fig. 6(i). The breakup of the dark core of the inner jet is accelerated and large-amplitude wave structures are formed. From these visualizations and the limited high-speed movies, it appears that, near to the injector exit area, the dark core of the inner jet is "pushed out" into the path of the outer jet flow and is then convected downstream away from

the injector. The dark core develops a cusp-like structure at a distance from the injector which subsequently separates from the attached region of the jet and ultimately disappears, becoming fully mixed with the outer-jet fluid.

Figure 6(ii) shows the impact of the velocity ratio and acoustic field on the coaxial jet under the low outer-jet temperature condition. As seen in the temperature measurements, the core jet also appears thicker here and the breakup seems to be of the fiber type. The jet responds to the acoustic field at all conditions with increasingly dramatic effects at higher velocity ratios. The length of the dark-core region (with the acoustic driver on) appears to be considerably larger than those seen in Fig. 6(i).

Images from a near-critical chamber pressure (~ 3.5 MPa) are shown in Fig. 7, and are arranged in the same fashion as those in Fig. 6. The droplets which were clearly present under the subcritical chamber pressure disappear as expected (see Chehroudi et al.[17]). Judging purely from the dark region of the jet, the effect of the acoustic field is less pronounced. However, from the high-speed movies taken with the Phantom camera and shown in the fourth row from the top of Fig. 8, the oscillation of the jet is quite visible due to the increased framing rate and the illumination arrangement, which allowed the outer-jet boundaries to be visualized. Figure 8 is composed of ten consecutive frames taken from an acquired high-speed movie of the jet. The first and second, the third and fourth, and the fifth and sixth pair of rows are at sub-, near-, and supercritical chamber pressures, respectively. In the first, third, and fifth rows the acoustic driver is *off*, and in the second, fourth, and sixth rows it is *on* at 3kHz. The framing rate was 18 kHz, producing a time interval of 55.6μs between frames. Previously reported[14] observations that the effect of the acoustic field was lesser under near- and supercritical pressures are still valid. However, the oscillations of the jet in the acoustic field under near- and supercritical conditions seen here were not previously detected because of the low framing rate available. The dark core (i.e. regions of high density) is the most visible structure, and as the density field becomes more uniform the discrimination of this effect diminishes.

Not immediately obvious in Fig. 8, but seen when played as a movie, the structures in the far-field background of the frame begin to oscillate laterally at the same frequency of the acoustic driver. One can measure the magnitude of these velocity fluctuations from the movies. Assuming that the acoustic wave in the chamber is a plane wave, the estimated pressure fluctuations from these measurements agreed with previously-measured pressure fluctuations. The velocity of the annular gas from the injector can also be estimated from these images. If one draws a line connecting the same structure seen in adjacent frames, the slope of this line is related to the axial convection

velocity of these structures (see Fig. 8). Similarly, if each of the individual images are rotated by 90 degrees, one can measure the radial velocity using the same method. Although further analysis is required, initial crude estimates are consistent with the computed values based on mass flow rate measurements.

By tracking the structures shown in Fig. 8 for the cases when the acoustic field is on, a possible explanation for the behavior of the jet is proposed. Once the dark high-density core of the inner jet leaves the injector, it experiences a force in the direction of the local acoustic field velocity at that moment, directing the fluid elements into the high-velocity of the outer-jet areas. While these elements are accelerated in the axial direction to speeds close to the outer-jet values, they nearly maintain the component of velocity in the wave propagation direction. However, once the dense region of these fluid elements (i.e. dark core) approaches the shear layer between the outer jet and chamber fluid, it experiences further mixing and heat transfer until it is no longer discernable. A fraction of these fluid elements from the dark core is convected downstream with the outer jet and experiences heat up and mixing until the elements eventually disappear into the rest of the background.

C. Dark Core Measurements

When a region of an image is referred to as a “dark core”, we simply are referring to an intact area of the jet, always defined by the inner jet, which clearly stands out in darkness level with respect to the remaining areas. This will be explained further in a quantitative term in this section. Some work that is relevant to the present study was performed by Glogowski et al.[23], in which a shear-coaxial injector was utilized with a design derived from a prototype SSME fuel preburner element using liquid nitrogen (LN2) and gaseous nitrogen (GN2). They stated that the length of the dark core in the acquired images increased significantly upon elevation of the chamber pressure from sub- to supercritical, at constant mass flow rates. They attributed this to the drop in the relative velocity between the inner and outer (annular) streams. Although temperature measurements were made somewhere downstream of the critical flow venturi location in the feed system, it was not clear how far upstream of the injector exit area this occurred. It is known that small changes in temperature in this thermodynamic region can bring about large changes in density, affecting the parameters, especially outer-to-inner velocity ratio, used to characterize the injector exit conditions. Close examination of the figures presented by Glogowski et al.[23] suggests that the dark core (that is, the flow issuing from the inner tube) of the jet actually appears to contract in length, while the visual impression of the outer annular flow is that it grows in length.

Measurements of both the liquid-core and dark-core lengths of a variety of different jets from photographs have been performed by others and reported in the past (see Eroglu et al.[7]). However, the measurement methods are often not discussed in sufficient detail. There are many difficulties in performing quantitative measurements from this quantity of images of a jet. For example, if using a strobe light for illumination purposes, the intensity of the background will most likely vary from shot to shot. Another difficulty is the selection of a criterion to assess the location where the core is broken up into separated pieces. It is then possible for two people to make different measurement judgments. Also, with the use of digital cameras capable of collecting thousands of images, a manual measurement becomes an extremely tedious and time consuming task. Therefore, in order to produce repeatable measurements, to account for the variability in the light source intensity, and to be able to process thousands of images, an algorithm is necessary for automated computer processing.

A judicious choice of a threshold level on the brightness scale of an image is necessary, and a single fixed value is not sufficient for all images to consistently determine the end or the break points of the dark core. Figure 9 is a sample image illustrating an automated thresholding procedure for determination of the length of the dark core. Figures 9 a, b, c, and d are, respectively, the untouched original photograph, the image threshold applied between 0-128 to indicate the injector, the image threshold applied between 128-929 to represent the dark core, and the image threshold applied between 929-4095 to depict the background. Figure 10 is the image histogram corresponding to Fig. 9 indicating the number of pixels versus a 12-bit gray scale level. The ability of an algorithm to successfully predict the proper threshold level is based on the physical implications of different gray level zones in an image as shown in Fig. 10. The peak to the left of the dashed line in this figure indicates the injector metal surface areas. With the object (i.e., injector) being backlit and the injector being absolutely opaque, one would expect that the zero level intensity should all represent the injector itself. However, the slight shift of the peak to a higher value is due to stray light being reflected by the chamber windows and other surfaces towards the injector which is then reflected back into the camera. The low number of pixels at gray level values between the dashed and dotted lines in Fig. 10 physically represents the dark core of interest, and the broad noisy peak at gray levels to the right of the dotted line in this figure defines the background.

As mentioned previously, variations of the light intensity from shot to shot are usually significant and a matter of concern. For example, in the case of Fig. 10, the threshold level distinguishing the end of the dark core and the beginning of the background is at a gray level of about 929. However, this value varies from shot to shot in a

sequence of images taken at the same operating conditions. Also, it varies more widely when the chamber conditions are changed due to differences in the refractive index field. Therefore, it is necessary to devise a methodology for an accurate and repeatable determination of the rise of the portion of the curve representing the contribution of the background in these images. More importantly, the outcome should conform to what human eyes determine to be the end of the dark core. To select the threshold level identifying the rise of the background, data from the histogram in this region was curve-fitted, using a non-linear Levenberg - Marquardt least squares algorithm, to a piece of a Gaussian function. This function is then differentiated and the point where the derivative of this curve is equal to e^{-1} was determined to be the threshold level corresponding to the dotted line shown in Fig. 10. Evidence to support the soundness and consistency of this algorithm is shown in detail by Davis et al.[13] and is visually shown in Fig. 9. For each condition, an averaged dark-core length was calculated based on analysis of each individual image within a set of 30 images and then averaging the results. The dark-core lengths are shown in Figs. 11(a) and 12(a) as a function of velocity ratio (*VR*). The RMS of the variations of this quantity is also shown in Figs. 11(b) and 12(b). Figures 11 and 12 present results for both higher and lower outer-jet temperatures of ~190 K and ~140 K, respectively. According to Eroglu et al.[7], the average of the length measured from individual images of a set can be regarded as the time average. It should be noted that, for each operating condition in this work, length measurements were also made from an averaged image of a set. In general, the length measured from the averaged image is slightly shorter than the average of the individual dark core values calculated in a given set.

Evident in Figs. 11(a) and 12(a) is the fact that the length of the dark core decreases as the chamber pressure is increased. The dark core provides an indication of high-density regions of the flow. A possible explanation of this effect is that, as the chamber pressure increases in the present system, the temperature of the inner jet also increases, causing the density of the inner jet to decrease and leading to a shortened length of the dark core, as seen in Fig. 5. Since the jet begins with a lowered density, less time is then required to fully mix the dark inner jet with the background. At a constant chamber pressure, as *VR* is increased, the length of the dark core decreases and approaches a plateau region. In a mean sense, when the dark core feels the imposed external acoustic field, the length of the core is shorter than or equal to the length when the acoustic driver is turned off. Under the near- and supercritical chamber pressures, as the *VR* parameter increases, the difference between the lengths of the dark core, measured with and without the acoustic field, diminishes. The RMS values of the dark-core length fluctuations, shown in Figs. 11(b) and 12(b), exhibit somewhat similar trends to those seen with their mean values. It is known

that for a liquid-fueled rocket, atomization and breakup processes, interactions between the propellant jets, droplet formation, and vaporization are all affected by the pressure and, particularly, velocity fluctuations. Also, for any chemically-reacting system, the rate at which energy is released is sensitive to the rate of change of temperature, density, pressure, and, of course, mixture ratio. It is then quite intuitive to relate, in some form, the RMS values of the dark-core length fluctuations to mixture ratio variations. On the other hand, a low RMS value can be interpreted as the jet's inherent steadiness and vice versa. Examination of Figs. 11b and 12b clearly shows that this property is drastically reduced as the velocity ratio is increased. Although these results are for a single injector, it is then quite possible that the observed improvement in combustion stability at higher values of velocity ratio is a result of the jet's inability to generate large mass flow rate fluctuations under these conditions, weakening a key feedback line for the self-excitation process. In temperature ramping exercises for stability rating of LOX/H_2 engines, the mass flow rate is usually maintained at a constant value[4]. Therefore, as the temperature of the H_2 is decreased during a ramping episode, the H_2 becomes more dense, which decreases the injector velocity ratio. The RMS plots shown here suggest that such a decline in this ratio amplifies the jet's inherent unsteadiness, providing a possible explanation for the engine's eventual arrival into an unstable zone as a temperature ramping test proceeds. Also, the observation reported by Wanhainen[11], who found that a decline in LOX density was de-stabilizing, can be explained in a similar manner. Unfortunately, due to small sample sizes, a distinct impact of the acoustic field on the RMS fluctuations is not evident in some cases. A sufficiently large sample size can be acquired through applications of high-resolution and high-speed cameras, such as the one acquired towards the latter part of this project.

Figure 13 shows a plot of L/D_1 versus M, with the diamond, circle, and up-triangle symbols representing sub-, near-, and supercritical pressures, respectively. The hollow and solid symbols represent the higher and lower outer-jet temperatures, respectively. The dashed and dotted curves in Fig. 13 represent the least squares fits following a functional form of $L/D_1 = C/M^n$, where C and n constant pair are 25 and 0.2 for subcritical pressures (dashed line) and 12 and 0.5 for near- and supercritical pressures. From Fig. 13, there is an apparent difference in the exponent of M between the subcritical and supercritical pressure data. Other researchers[24-29] observed a dependence of core length on M ranging from $M^{-0.5}$ to $M^{-0.13}$. For a coaxial jet where there is a single phase and therefore no surface tension, such as the water – water experiments of Rehab et al.[25] and the gas – gas experiments of Favre-Marinet and Schetti[27], the dependence of the core length was $M^{-0.5}$, which is consistent with the present near-critical and supercritical results. Chehroudi et al.[17] noted a difference in behavior of subcritical and supercritical jets. They

showed that the initial growth rate of a supercritical single round-jet behaved like a variable-density gas jet. Figure 13 gives evidence to the fact that supercritical single-component coaxial jets behave like their subcritical single-phase counterparts. Caution should be exercised when extrapolating these results to systems containing multiple chemical species. A system which contains a mixture of chemical species, at a pressure greater than the critical pressure of any of the individual components, may in fact still be below the critical pressure of the mixture. For example, the critical pressures of carbon dioxide (CO_2), toluene, and H_2 are 7.49 MPa, 4.1 MPa, and 1.3 MPa, respectively. A mixture of approximately 95% by mole of CO_2 and 5% toluene has a critical pressure of 10.5 MPa, and a 90.75%, 1.55 %, 7.70%, mixture of CO_2, toluene, and H_2, respectively, has a critical pressure of 11.4 MPa.[30]

IV. Summary and Conclusions

Radial mean temperature measurements were made from a coaxial jet under sub-, near-, and supercritical pressures at a fixed axial location very near the injector exit plane at a variety of outer-to-inner jet velocity ratios. Two nominal temperature levels (low (~135 – 140 K) and high (~185 – 200 K)) were selected for the outer jet to investigate the impact of the velocity ratios and acoustic field on the coaxial jet considering a nominal cryogenic temperature for the inner jet. To the best of the authors' knowledge, measurements at this level of detail have not been previously performed. True exit velocity ratios, as opposed to ratios based on upstream values, can now be calculated with sufficient accuracy, especially under near- and supercritical conditions, to aid in interpretation of the results. Under subcritical pressures, temperature profiles exhibit a top-hat behavior at two distinct levels with an abrupt transition from a high (liquid-like for the inner jet) to a low value representative of compressed gases. The transition point is somewhere in the region between the outer and the inner jet flows. Large changes in velocity ratio had no impact on these profiles at the low outer-jet temperature, whereas the location of the transition point was affected under the higher outer-jet temperature. At near- and supercritical chamber pressures, the inner jet loses its top-hat shape and the temperature profiles exhibit a more gradual transition from the inner to outer jet.

Backlit images were taken at both low (10 Hz) and high speeds (18 kHz) with and without the acoustic driver turned on at 3 kHz. Using images taken at high framing rates, velocity fluctuations in the chamber background fluid and within the jets were observed when the acoustic driver was on. Velocities can be measured by tracking isolated structures in these images. Initial crude measurements of the velocities agreed with the predicted values.

A prominent feature seen in most of the images in the study is the existence of a high-density region, referred to as the “dark core”, which is defined by the fluids in the inner jet. An automated method for measurement of the dark core was produced to enable rapid analysis of a large number of images in a repeatable and consistent manner. It is seen that the dark-core length decreases at higher chamber pressures, due to the combined effects of inner-tube heat transfer and better inter-jet mixing. As the velocity ratio increases at a constant chamber pressure, the length of the dark core shortens and asymptotically approaches a constant value. This constant value appears to be different for subcritical pressures. Results show the dependence of the outer-to-inner jet momentum ratio to an exponent, with the exponent having a different value for subcritical pressures as opposed to near- and supercritical pressures. The exponent for near- and supercritical pressures is consistent with previous measurements of the potential core for single-phase systems.

It is hypothesized that a connection to combustion instability can be obtained from the data analyzed thus far by way of the magnitude of the RMS values of the dark-core length fluctuations. It is possible that decreases in the fluctuation levels, which were shown here to occur at higher velocity ratios, could weaken a key feedback mechanism for the self-excitation process that is believed to drive the combustion instability in rocket engines. This offers a possible means for improvements in our understanding of combustion instability experienced in engines under higher outer-to-inner jet velocity ratios. Additional analysis and data acquisition are planned to further investigate this initial finding.

References

[1]Culick F. E. and Yang, V., “Overview of Combustion instabilities in Liquid-Propellant Rocket Engines,” Liquid Rocket Engine Combustion Instability, edited by V. Yang and W. Anderson, Progress in Astronautics and Aeronautics, AIAA, Washington, DC, 1995, pp. 3-38.

[2]Harrje, D. T., and Reardon, F. H. (eds.) “Liquid Propellant Rocket Combustion Instability,” NASA SP-194, 1972, pp. 17-19.

[3]Vingert, L., Gicquel, P., Lourme, D., and Ménoret, L., “Coaxial Injector Atomization,” Liquid Rocket Engine Combustion Instability, edited by V. Yang and W. Anderson, Progress in Astronautics and Aeronautics, AIAA, Washington, DC, 1995, pp.145-190.

[4]Hulka, J., and Hutt, J., “Liquid Oxygen / Hydrogen Instability Phenomena,” Liquid Rocket Engine Combustion Instability, edited by V. Yang and W. Anderson, Progress in Astronautics and Aeronautics, AIAA, Washington, DC, 1995, pp. 39-72.

[5]Rayleigh, J. S. W “On the instability of Jets,” Proceedings of London Mathematical Society, Vol. 10, 1878.

[6]Lefebvre, A. H., *Atomization and Sprays*, Hemisphere, New York, 1989.

[7]Eroglu, H., Chigier, N., and Farago, Z., "Coaxial Atomizer Intact Lengths," Physics of Fluids A, Vol. 3, No. 2, Jan. 1991, pp. 303-308.

[8]Lasheras, J. C., and Hopfinger, E. J., "Liquid Jet Instability and Atomization in a Coaxial Gas Stream," Annual Review of Fluid Mechanics, Vol. 32, 2000, pp. 275-308.

[9]Miesse, C. C., "The effect of Ambient Pressure Oscillations on the Disintegration and Dispersion of a Liquid Jet," Jet Propulsion, Vol. 25, Oct. 1955, pp. 525-530,534

[10]Buffum, F. G., and Williams, F. A., "Response of Turbulent Jets to Transverse Acoustic Fields," Proceedings of the 1967 Heat Transfer and Fluid Mechanics Institute, edited by P. A. Libby, D. B. Olfe, and C. W. Van Atta, 1967, pp. 247-276.

[11] Wanhainen, J. P., Feiler, C. E., and Morgan, C. J., "Effect of Chamber Pressure, Flow per Element, and Contraction Ratio on Acoustic-Mode Instability in Hydrogen – Oxygen Rockets," NASA TN D-4733, August 1968.

[12]Heidmann, M. F., "Oxygen-Jet Behavior during Combustion Instability in a Two-Dimensional Combustor," NASA TN D-2725, March 1965.

[13]Davis, D. W., Chehroudi, B., and Sorensen, I. "Measurements in an Acoustically Driven Coaxial Jet Under Supercritical Condition," 43rd AIAA Aerospace Sciences Meeting & Exhibit, AIAA, Washington, DC, 10-13 Jan. 2004.

[14]Davis, D. W. and Chehroudi, B., "The effects of Pressure and Acoustic Field on a Cryogenic Coaxial Jet," 42nd AIAA Aerospace Sciences Meeting & Exhibit, AIAA, Washington, DC, 5-8 Jan. 2004.

[15]Chehroudi, B., Davis, D. W., and Talley, D. G., "Initial Results from A Cryogenic Coaxial Injector In An Acoustic Field," 41st AIAA Aerospace Sciences Meeting & Exhibit, AIAA, Washington, DC, 6-9 Jan. 2003.

[16]Chehroudi, B., Cohn, R., and Talley, D. G., "Cryogenic Shear Layers: Experiments and Initial Growth Rates of Round Cryogenic Jets at Subcritical and Supercritical Pressures," International Journal of Heat and Fluid Flow, Vol. 23, 2002, pp. 554-563.

[17]Chehroudi, B., Talley, D. G., and Coy, E. B. "Visual Characteristics and Initial Growth Rates of Round Cryogenic Jets at Subcritical and Supercritical Pressures," Physics of Fluids, Vol.4, No. 2, Feb. 2002. pp. 850-861.

[18]Chehroudi, B., Cohn, R., Talley, D. G, and Badakhsan, A., "Raman Scattering Measurements in the Initial Region of Sub- and Supercritical Jets," 36th AIAA/ASME/SAE/ASEE Joint Propulsion Conference and Exhibit, AIAA, Washington, DC, 17-19 Jul. 2000.

[19]Chehroudi, B., Talley, D., and Coy, E. B., "Initial Growth Rate and Visual Characteristics of a Round Jet into a Sub- to Supercritical Environment of Relevance to Rocket, Gas turbine, and Diesel Engines," 37th AIAA Aerospace Science Meeting and Exhibit, AIAA, Washington, DC, 11-14 Jan. 1999.

[20]Chehroudi, B., Talley, D. G., and Coy, E. B., "Fractal Geometry and Growth Rate Changes of Cryogenic Jets Near the Critical Point," 35th AIAA/ASME/SAE/ASEE Joint Propulsion Conference and Exhibit, AIAA, Washington, DC, 20-24 Jun. 1999.

[21]REFPROP, Reference Fluid Thermodynamic and Transport Properties, Software Package, Ver. 7.0, NIST, U.S. Department of Commerce, Gaithersburg, MD, 2002.

[22]Faragó, Z., and Chigier, N., "Morphological Classification of Disintegration of Round Liquid Jets in a Coaxial Air Stream," Atomization and Sprays, Vol. 2, 1992, pp. 137-153.

[23]Glogowski, M., Bar-Gil, M., Puissant, C., Kaltz, T., Milicic, M., and Micci, M., "Shear Coaxial Injector Instability Mechanisms" 30th AIAA/ASME/SAE/ASEE Joint Propulsion Conference, AIAA, Washington, DC, 27-29 Jun. 1994.

[24]Lasheras, J. C, Villermaux, E., and Hopfinger, E. J., "Breakup and Atomization of a Round Water Jet by a High Speed annular Air Jet," J. Fluid Mech. Vol. 357, 1998, pp. 351-379.

[25]Rehab, H., Villermaux, E., Hopfinger, E. J., "Flow Regimes of Large Velocity Ratio Coaxial Jets," J. Fluid Mech., 1997, pp.357-381.

[26]Raynal, L. Instabilite et entrainment a l'interface d'une couche de mélange liquid-gaz, Thèse de Doctorat, Universite Joseph Fourier, Grenoble, France, 1997. In Ref. 8.

[27]Favre-Marinet, M., and Camano Schettini, E. B., "The Density Field of Coaxial Jets with Large Velocity Ratio and Large Density Differences," International Journal of Heat and Mass Transfer, Vol. 44, 2001, pp. 1913-1924.

[28]Englebert, C., Hardalupas, Y., and Whitlaw, J. H., "Breakup Phenomena in Coaxial Air-Blast Atomizers," *Proc. R. Soc.*, Vol. 451, London, 1995, pp. 189-229.

[29]Porcheron, E.., Carreau, J. L., Prevost, L., LeVisage, D., and Roger, F., "Effect of Density on Coaxial Liquid Jet Atomization," Atomization and Sprays, Vol. 12, 2002, pp. 209-227.

[30]Zhang, H, Liu, Z., and Han, B., "Critical Points and Phase Behavior of Toluene - CO_2 and Toluene-H_2 -CO_2 mixture in CO_2 – Rich Region," Journal of Supercritical Fluids, Vol. 18, 2000, pp. 185-192.

Figures and Table

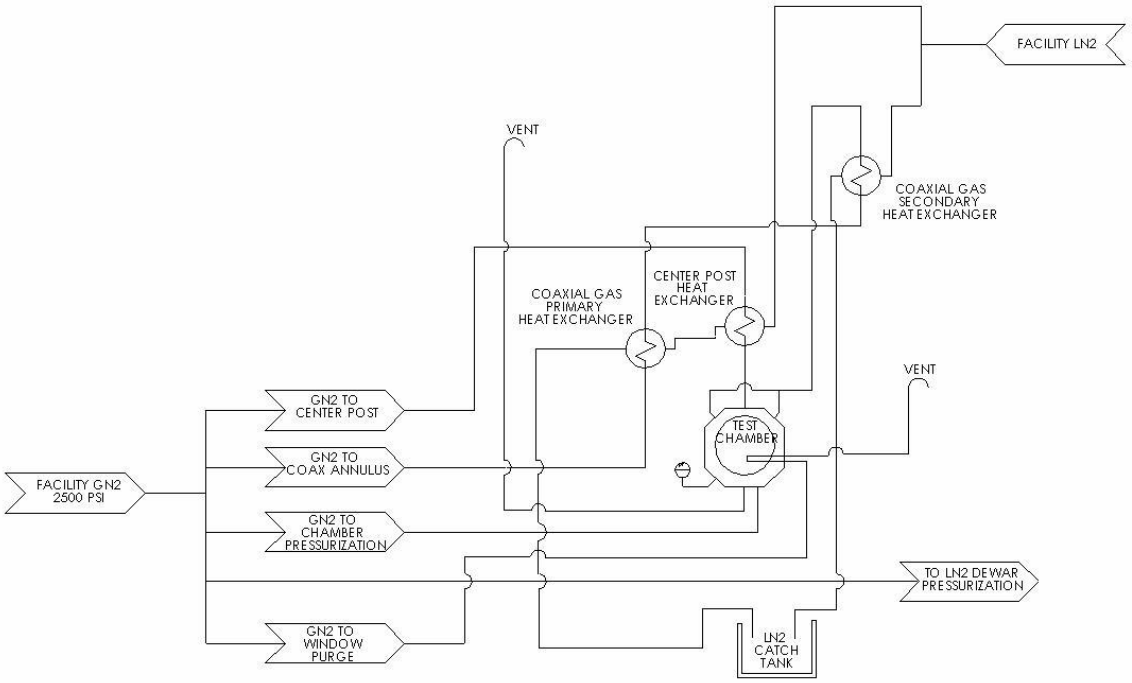

Figure 1. Schematic diagram of the Supercritical Facility at AFRL

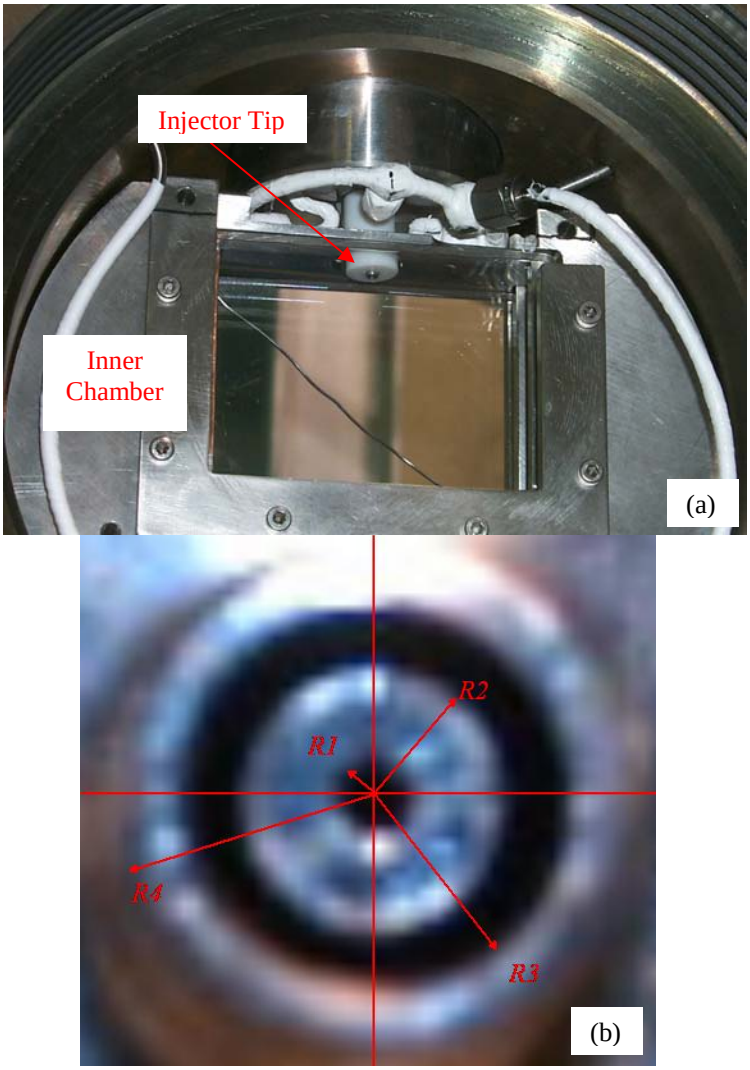

Figure 2. (a) View of inner chamber; (b) Close-up image of the coaxial injector tip area, the dimensions of the injector are: R_1 = 0.25 mm, R_2 = 0.79 mm, R_3 = 1.21 mm, and R_4 = 1.59 mm.

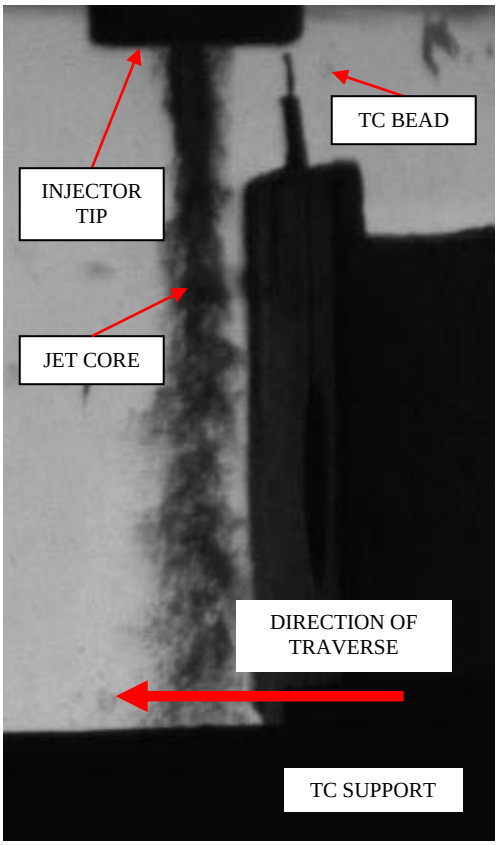

Figure 3. Thermocouple (TC) and the support mechanism used to perform radial temperature measurements in the coaxial jet. The thermocouple bead diameter is 0.10 mm. The resolution of the radial distance is 0.01 mm. The distance from the injector exit plane to the thermocouple bead is 0.14 mm or 0.28 D_1.

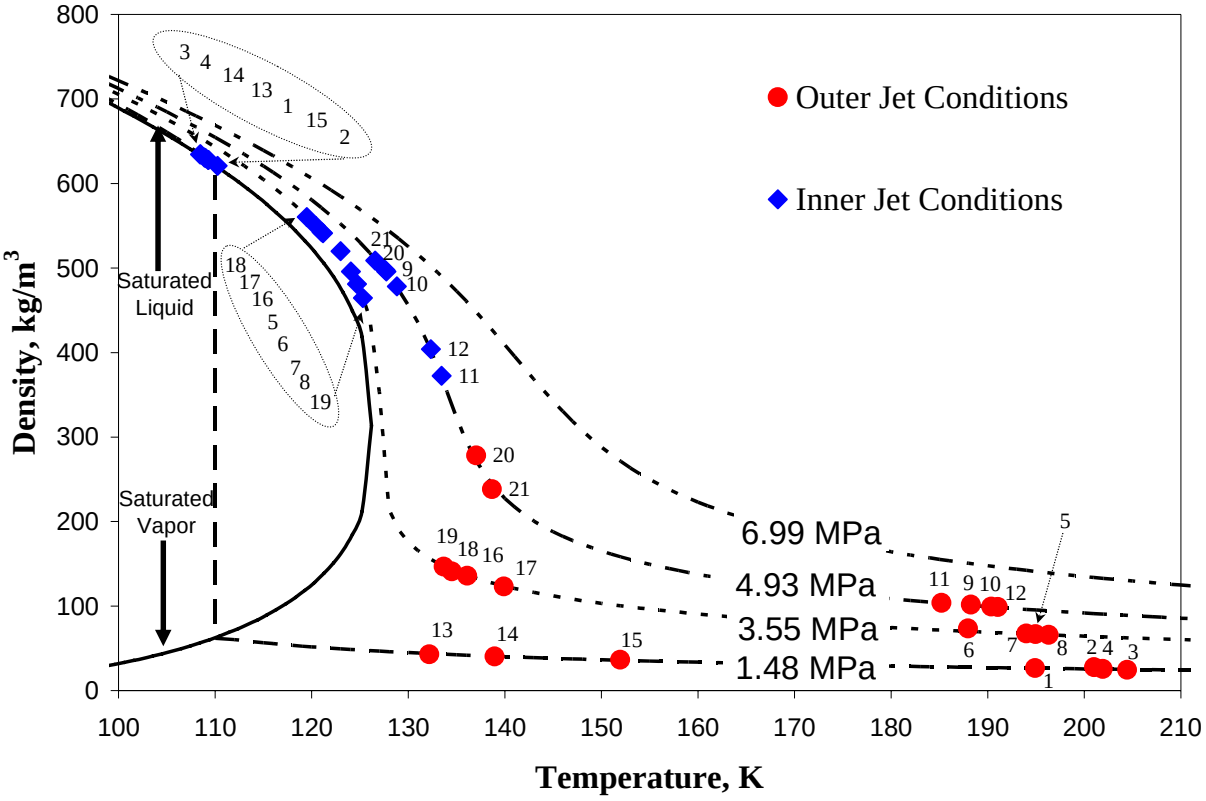

Figure 4. Thermodynamic conditions of the data. The numbers near the points indicate the respective cases shown in Table 1.

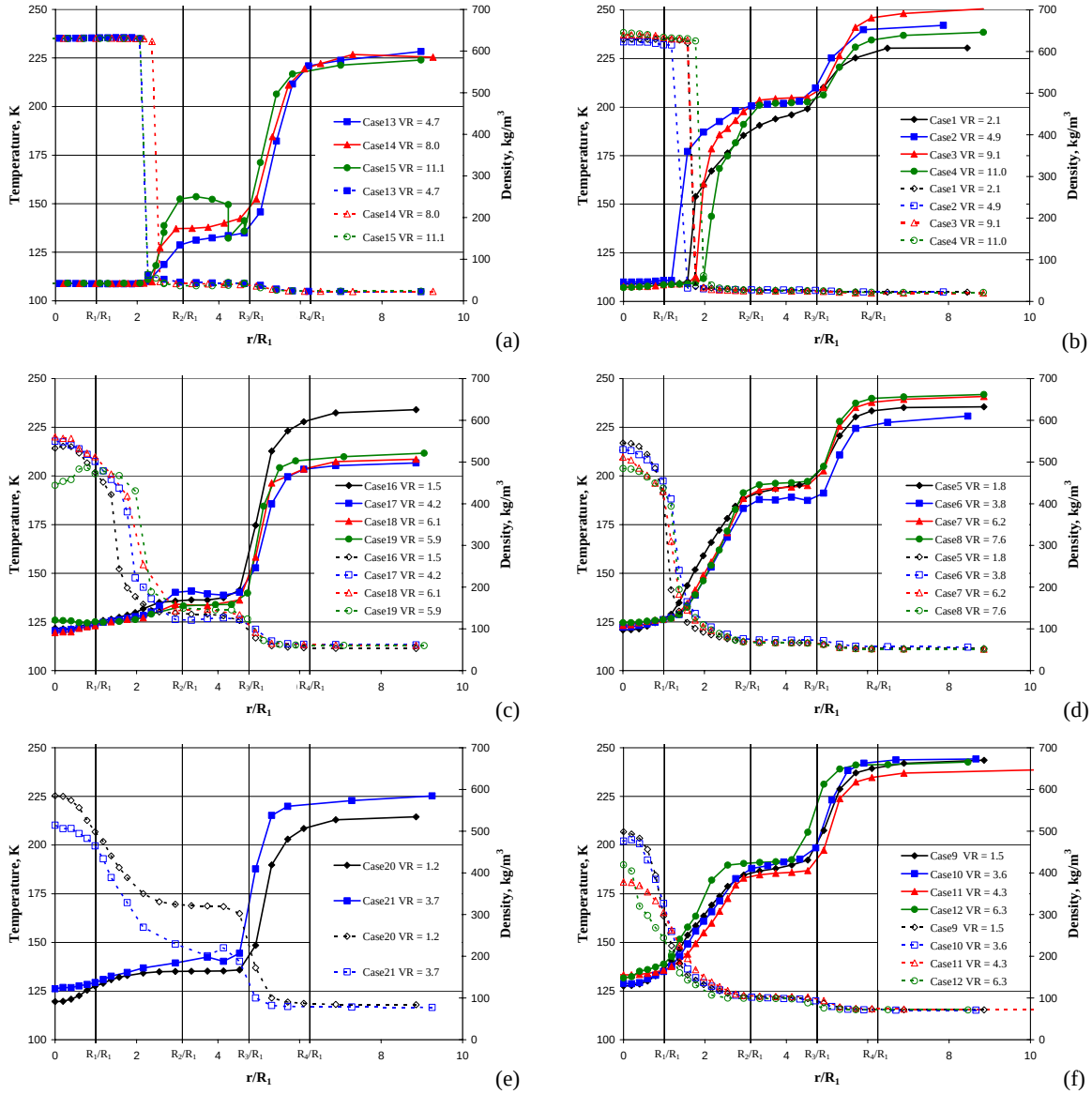

Figure 5. Radial profiles of the measured average temperature and calculated density. Conditions of cases are listed in Table 1. The chamber pressure in the top row is ~ 1.5 MPa , in the middle row is ~ 3.5 MPa , and in the bottom row is ~ 4.9 MPa. The nominal outer jet temperatures in the left and right columns are about 140 K and 190K, respectively. See Table 1 for exact values.

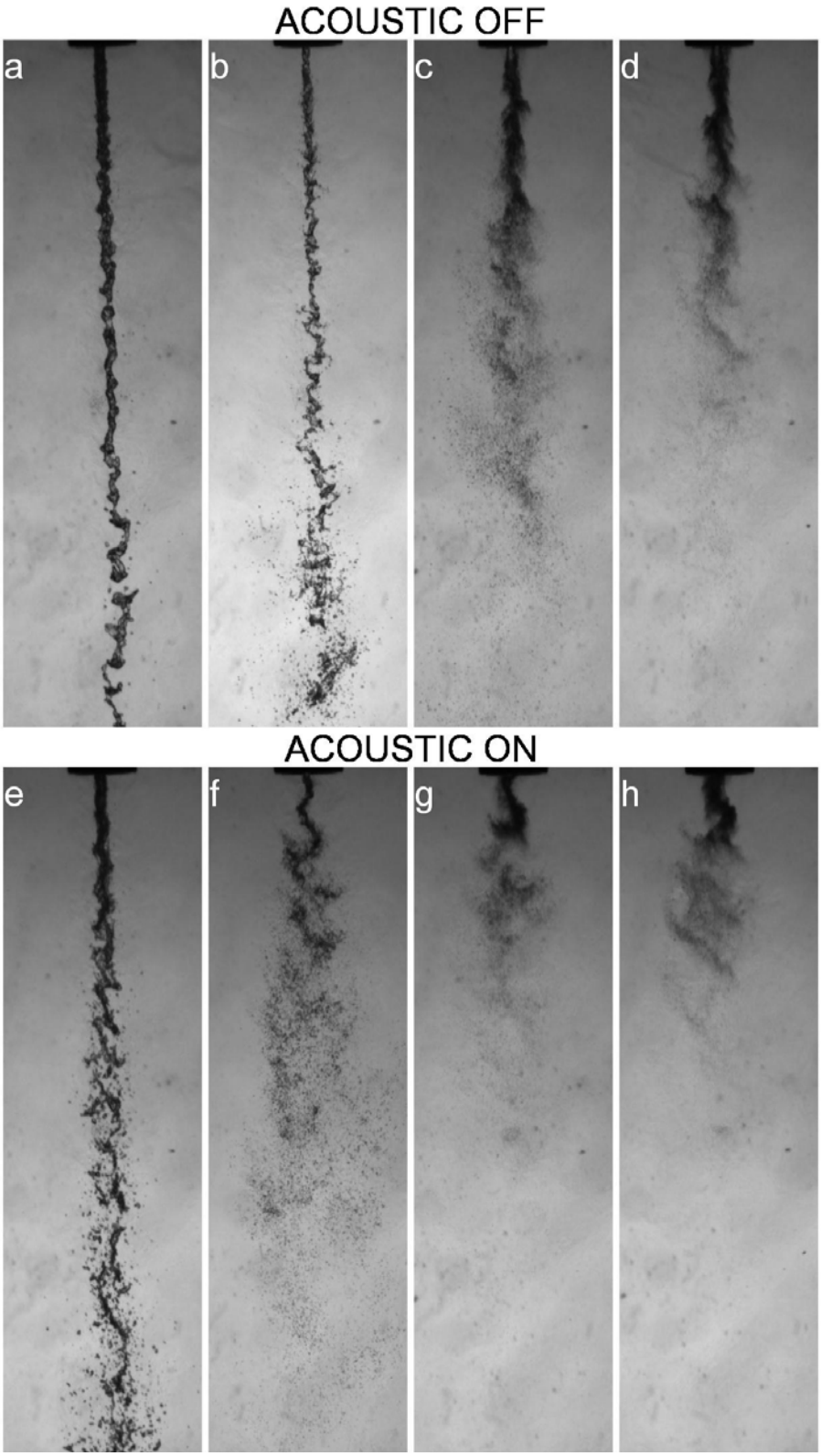

Figure 6(i). Backlit images of coaxial jet at subcritical chamber pressure (~1.5MPa) and at the higher outer jet temperature (~ 190 K) corresponding to cases 1-4 from left to right. The acoustic driver is *off* for images in the top row and *on* for the bottom row at ~*3 KHz*. The velocity ratio increases from left to right.

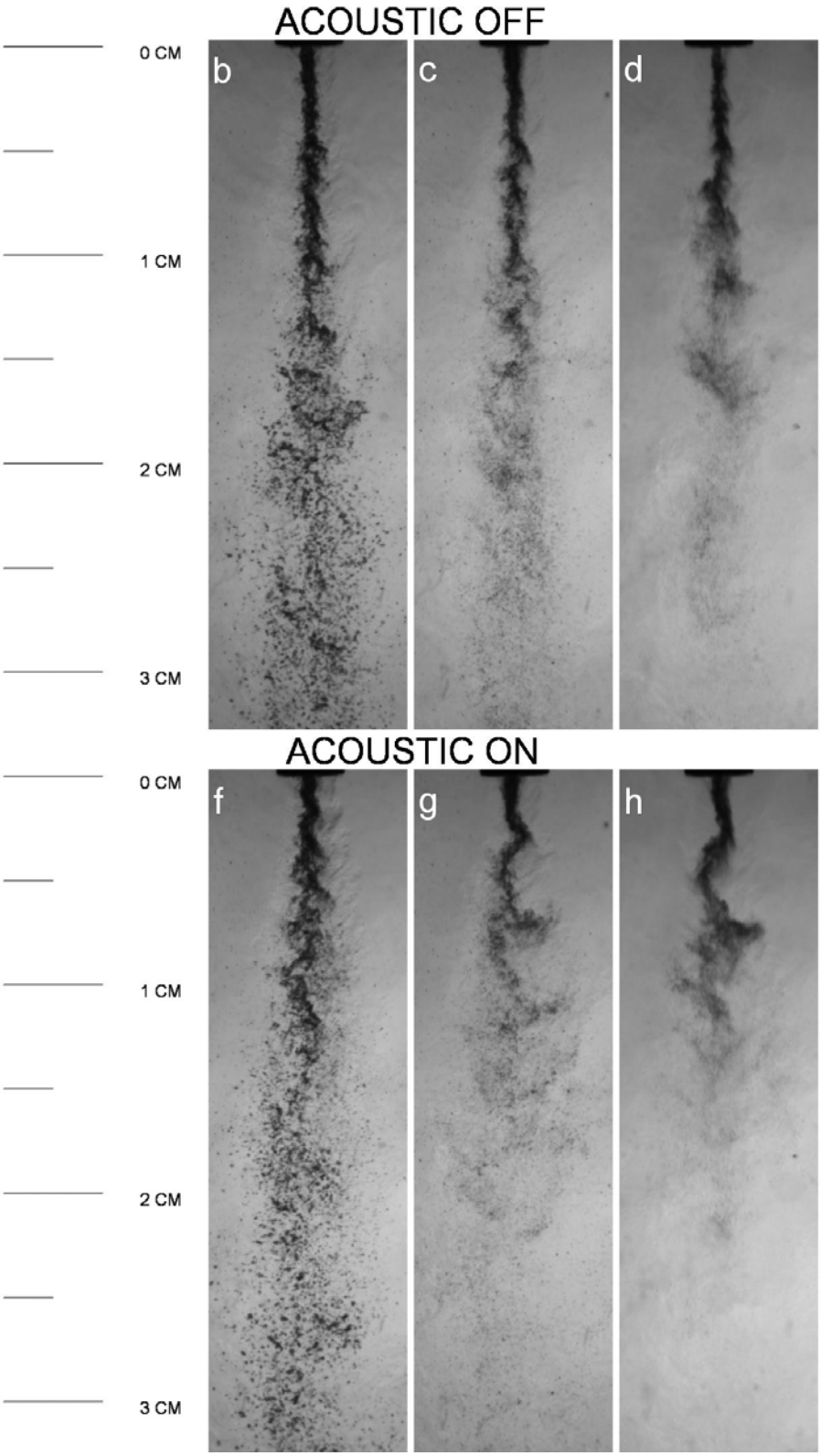

Figure 6(ii). Backlit images of coaxial jet at subcritical chamber pressure (~1.5MPa) and at the lower outer jet temperature (~ 140 K) corresponding to cases 13-15 from left to right. The acoustic driver is off for images in the *top row and on for the bottom row* at *~3 KHz*. The velocity ratio increases from left to right. The lowest flow rate condition was unattainable experimentally.

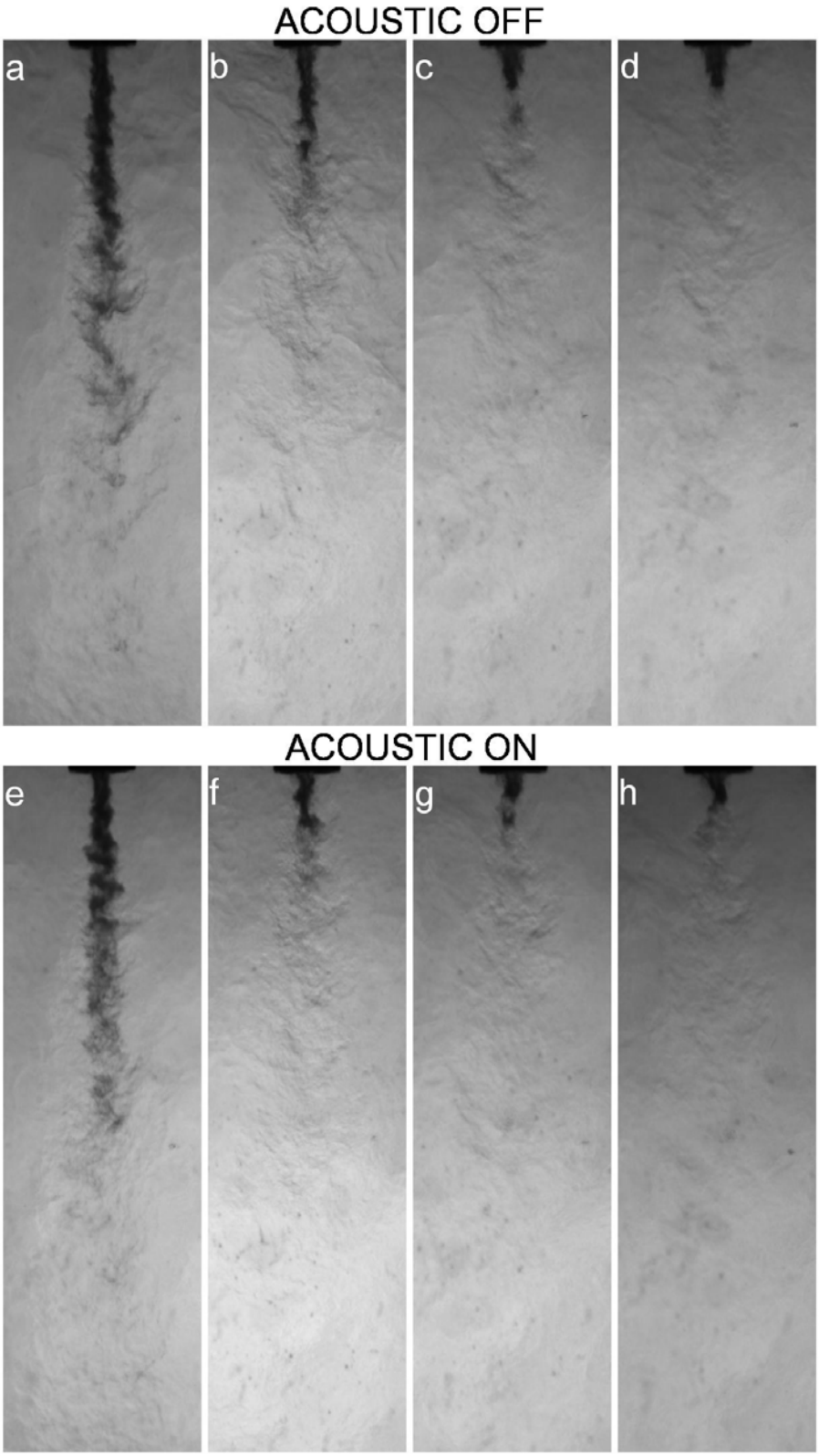

Figure 7. Backlit images of a coaxial jet at nearcritical chamber pressure (~3.5 MPa) and at a high outer jet temperature (~ 190 K) corresponding to cases 5-8 from left to right. Images in the *top row* the acoustic driver is *off*, and the *bottom row* the acoustic driver is *on* at *~3 KHz*. The velocity ratio increases from left to right.

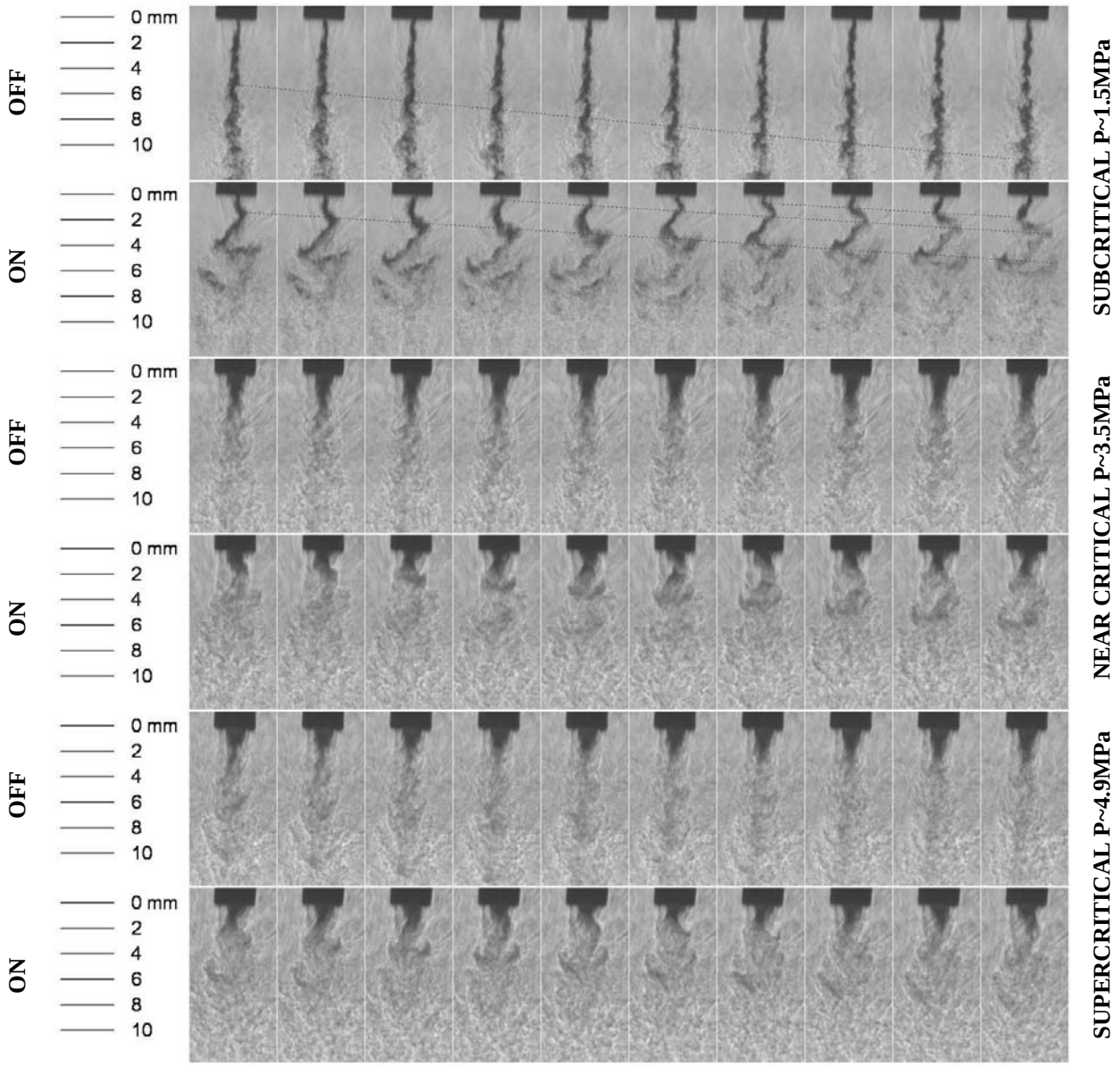

Figure 8. Consecutive frames from high-speed shadowgraph images of case 3, 7, and 11 (from Table 1) with the acoustic driver turned on and off. Time increases from left to right with an interval of $55.6\mu s$ between frames. The first two rows are at a subcritical chamber pressure (~ 1.5 MPa, case 19), the third and fourth rows are at a near-critical chamber pressure (~ 3.5 MPa), and the fifth and sixth rows are at a supercritical chamber pressure (~ 4.9 MPa). The acoustic driver is *off* for the first, third, and fifth rows and on for the second, fourth, and sixth at ~ 3 kHz.

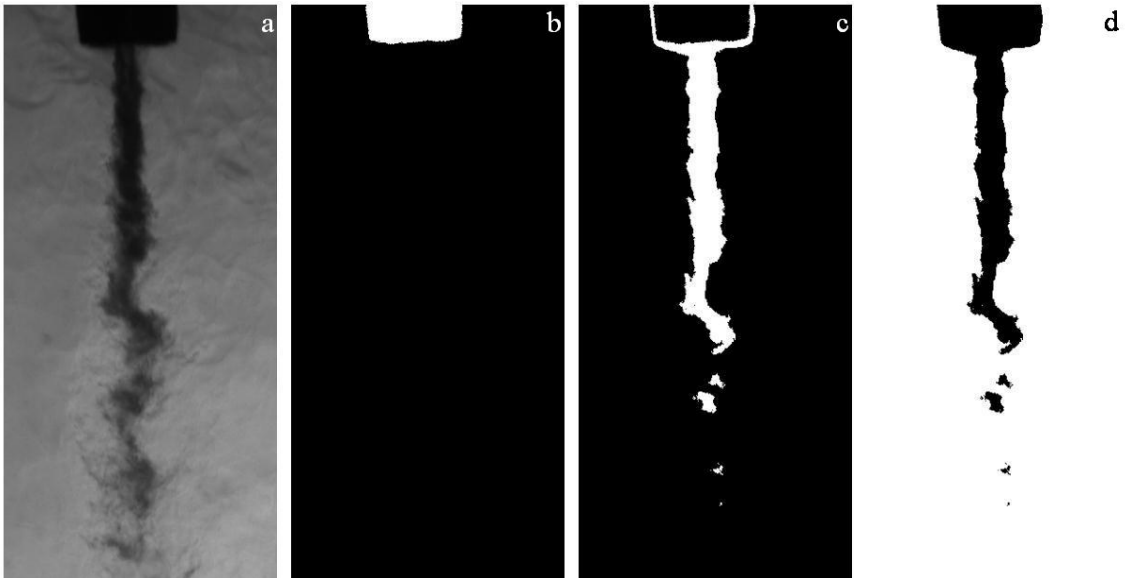

Figure 9. Sample images indicating the effect of threshold levels. Images a, b, c, and d are the original photograph, threshold applied between 0-128 indicating the injector, threshold applied between 128-929 indicating the dark core, and threshold applied between 929-4095 indicating the background, respectively.

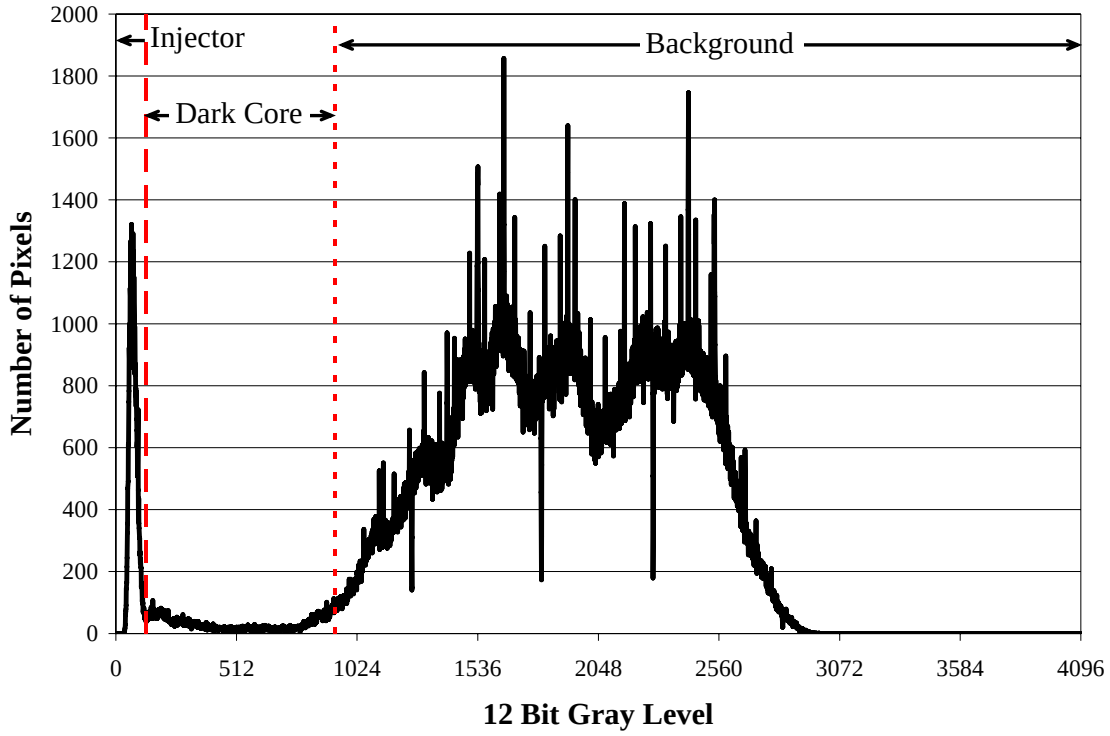

Figure 10. Histogram for the image in Fig. 9. The peak between 0-128 (the dashed line) gray levels represent the injector, the low region between 128-929 (between the dashed line and the dotted line) indicates dark core, and the noisy broad peak greater than 929 (beyond the dotted line) indicates the background.

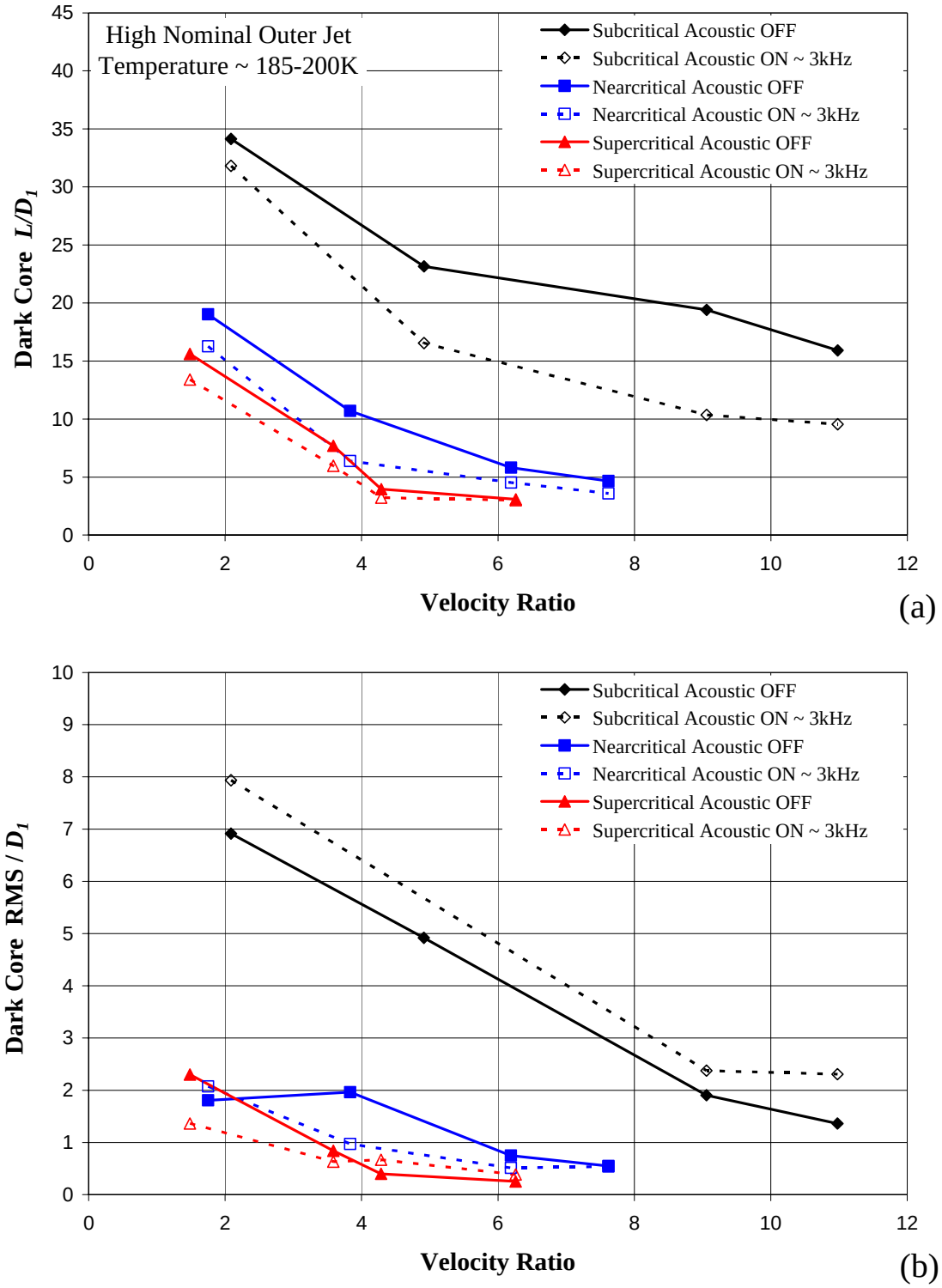

Figure 11. Plot of the dark core length (a) and the RMS of the variations (b) normalized by the inner diameter. The solid symbols and lines represent the data for when the acoustic driver is *off*, and the hollow symbols and dotted lines show the data when the acoustic driver operates at ~ 3kHz. The diamond, square, and up-triangle symbols are for cases 1-4, 5-8, and 9-12, respectively. All cases are for the higher nominal outer-jet temperature of ~190 K. Data for each of the cases is listed in Table 1.

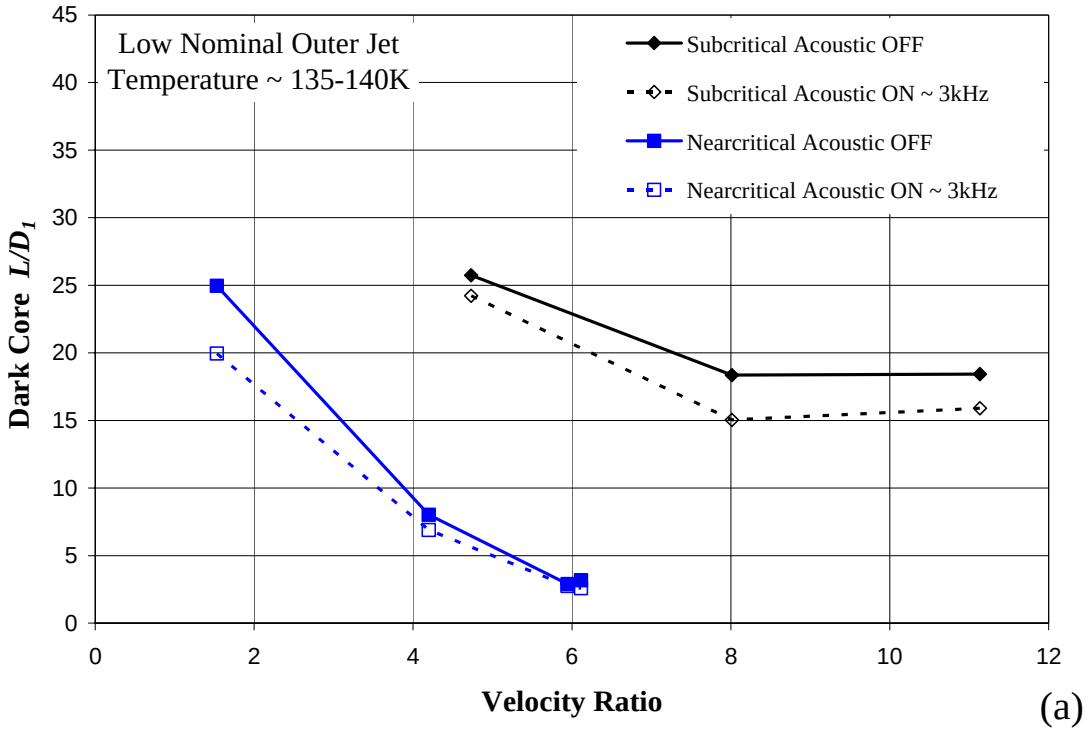

(a)

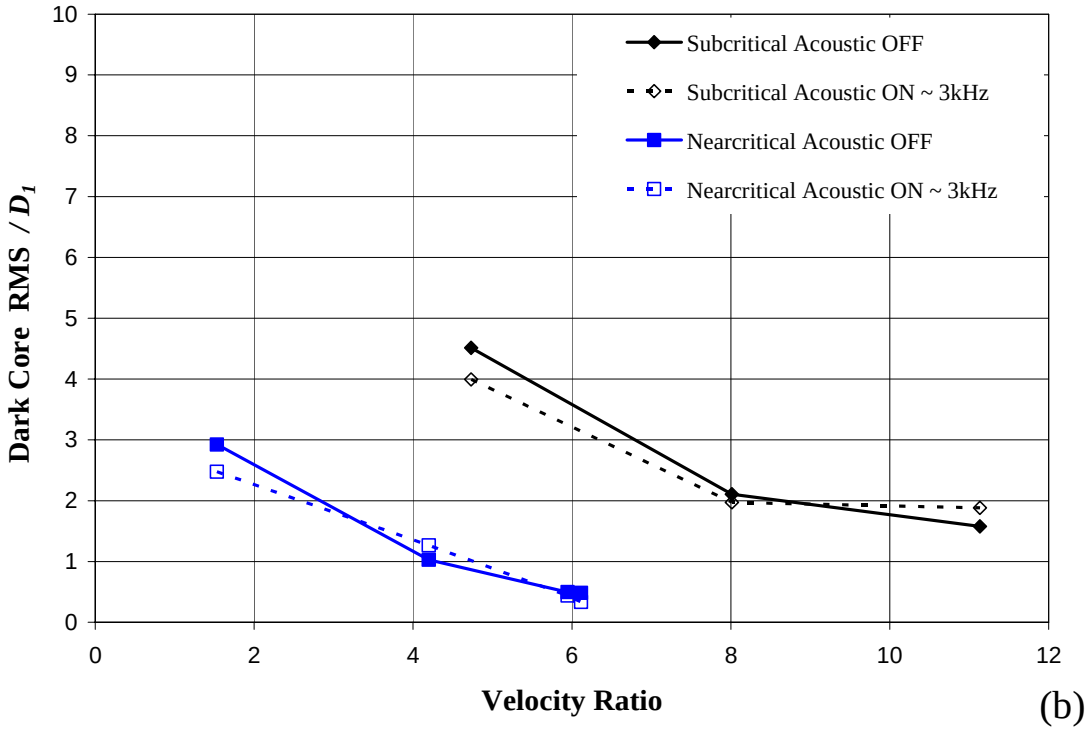

(b)

Figure 12. Plot of the dark core length (a) and the RMS of the variations (b) normalized by the inner diameter. The solid symbols and lines represent data for when the acoustic driver *off*, and the hollow symbols and dotted lines show results when the acoustic driver is operated at ~ 3kHz. The diamond and square symbols are for cases 13-15 and 16-19, respectively. All cases are for the lower nominal outer-jet temperature of ~140 K. Data for each of the cases is listed in Table 1.

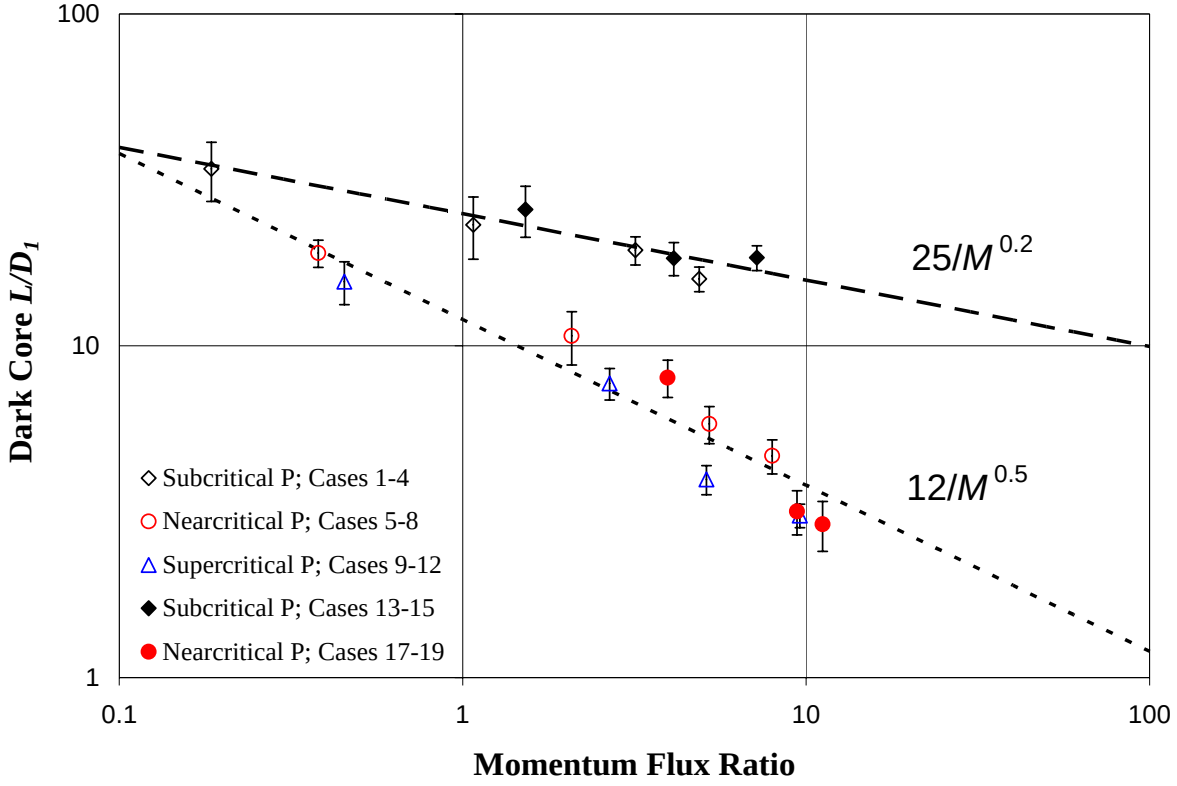

Figure 13. Dark core length versus momentum flux ratio. The diamond, circle, and up-triangle symbols represent sub-, near-, and supercritical chamber pressure, respectively. The hollow symbols are at a higher outer-jet temperature (~190 K) and solid symbols are at a lower outer-jet temperature. The dashed line is $26/M^{0.2}$ and the dotted line is $13/M^{0.5}$.

Table1. Data conditions for the various cases.

Case	Chamber	Outer Jet	Inner Jet	Chamber	Outer Jet	Inner Jet	Chamber	Outer Jet	Inner Jet	Outer Jet	Inner Jet	Outer Jet	Inner Jet	VR	M	Acoustic	L/D_1
	P	*m*	*m*	T	T	T	ρ	ρ	ρ	U	U	Re	Re	o / i	o / i	Frequency	
	(MPa)	(mg/s)	(mg/s)	(K)	(K)	(K)	(kg/m^3)	(kg/m^3)	(kg/m^3)	(m/s)	(m/s)	($x10^4$)	($x10^4$)			(kHz)	
1	1.49	316	276	238	195	109	21.4	26.7	627.9	4.5	2.2	0.77	1.21	2.1	0.2	2.96	34.1
2	1.59	787	280	248	201	110	21.9	27.6	620.8	10.9	2.2	1.87	1.27	4.9	1.1	2.99	23.1
3	1.45	1271	281	249	204	108	19.9	24.6	634.5	19.8	2.2	2.99	1.20	9.1	3.2	2.98	19.4
4	1.49	1602	280	237	202	108	21.6	25.7	634.6	23.9	2.2	3.81	1.19	11.0	4.9	2.98	15.9
5	3.56	801	287	238	195	121	51.9	66.9	541.1	4.6	2.6	1.86	1.76	1.8	0.4	2.99	19.0
6	3.70	2001	287	233	188	123	55.4	73.4	520.0	10.4	2.7	4.73	1.90	3.8	2.1	2.99	10.7
7	3.57	3132	288	235	194	124	53.1	67.5	495.9	17.8	2.9	7.28	2.08	6.2	5.2	2.95	5.8
8	3.55	3899	290	235	196	125	52.6	66.0	481.1	22.6	3.0	9.00	2.20	7.6	8.0	2.96	4.7
9	4.97	1156	294	240	188	128	72.6	101.8	495.9	4.4	2.9	2.61	2.11	1.5	0.5	3.06	15.6
10	4.95	2821	293	237	190	129	73.4	99.5	478.3	10.9	3.0	6.34	2.24	3.6	2.7	2.99	7.7
11	4.94	4558	296	228	185	133	77.1	103.8	372.5	16.8	3.9	10.39	3.20	4.3	5.1	2.98	4.0
12	4.94	5812	295	233	191	132	75.0	98.8	404.0	22.5	3.6	13.05	2.88	6.3	9.6	2.95	3.1
13	1.45	1159	280	231	132	109	21.5	42.9	630.8	10.3	2.2	3.82	1.21	4.7	1.5	2.94	25.7
14	1.47	1858	281	224	139	109	22.6	40.4	630.0	17.6	2.2	5.90	1.22	8.0	4.1	2.94	18.4
15	1.50	2328	280	219	152	109	23.6	36.4	627.9	24.5	2.2	6.90	1.23	11.1	7.2	2.91	18.4
16	3.54	1436	291	228	136	121	54.6	135.8	542.4	4.1	2.6	3.84	1.78	1.5	0.6	3.06	-
17	3.53	3521	291	202	140	120	63.2	123.1	549.9	11.0	2.6	9.49	1.73	4.2	3.9	3.05	8.0
18	3.52	5731	289	197	135	119	65.2	141.0	560.4	15.6	2.5	15.26	1.65	6.1	9.4	3.06	3.2
19	3.54	7076	293	197	134	125	65.7	146.8	464.5	18.5	3.1	18.66	2.35	5.9	11.2	3.01	2.9
20	4.97	2603	293	218	137	128	82.2	278.1	497.7	3.6	2.9	4.75	2.09	1.2	0.8	2.95	9.8
21	4.88	6547	296	203	139	127	88.8	238.4	508.8	10.5	2.9	13.31	2.03	3.7	6.3	2.99	-

Acknowledgments

The authors would like to acknowledge Dr. Douglas Talley for his support and contributions with this ongoing project. Also, the authors would like to acknowledge Mr. Mike Griggs for his valuable contributions in the improvements to the experimental facility. Lt. Matthew Raskie, Mr. Earl Thomas, Mr. Randy Harvey, Mr. David Hill, and Mr. Mark Wilson are thanked for their efforts. Additionally, Ms. Jennie Paton is thanked for making literature available in a timely manner. A great appreciation is extended to Mr. Steven Martin for loaning the authors the Phantom Camera. The first author would like to thank his thesis advisor, Dr. R. J. Santoro, for permitting his thesis work to be performed off-campus at AFRL. This work is sponsored by the Air Force Office of Scientific Research under Dr. Mitat Birkan, program manager.